communications
earth & environment

ARTICLE

https://doi.org/10.1038/s43247-021-00135-5 OPEN

# Fractional crystallization causes the iron isotope contrast between mid-ocean ridge basalts and abyssal peridotites

Yanhong Chen [1,2]✉, Yaoling Niu [1,2,3,4]✉, Meng Duan[3,4], Hongmei Gong[3,4] & Pengyuan Guo[3,4]

The iron isotope contrast between mid-ocean ridge basalts and abyssal peridotites is far greater than can be explained by mantle melting alone. Here we investigate a suite of mid-ocean ridge magma chamber rocks sampled by the Ocean Drilling Project Hole 735B in the Atlantis Bank of the Indian Ocean. We report major and trace element geochemistry from these rocks and measure their iron isotope compositions to investigate the potential role of fractional crystallization during melt evolution. We observe a large range of $\delta^{56}$Fe that defines a significant inverse curvilinear correlation with bulk rock MgO/FeO$^{T}$. These data confirm that $\delta^{56}$Fe in the melt increases as fractional crystallization proceeds but, contrary to expectation, $\delta^{56}$Fe continues to increase even when oxides begin to crystallize. We conclude that iron isotope fractionation through fractional crystallization during the evolution of mid-ocean ridge basalts from abyssal peridotites reconciles the disparity in isotopic compositions between these two lithologies.

[1] School of Earth Science and Resources, China University of Geosciences, Beijing, China. [2] Department of Earth Sciences, Durham University, Durham, UK. [3] Key Laboratory of Marine Geology and Environment, Institute of Oceanology, Chinese Academy of Sciences, Qingdao, China. [4] Qingdao National Laboratory for Marine Science and Technology, Qingdao, China. ✉email: chenyh@cugb.edu.cn; yaoling.niu@durham.ac.uk

Our knowledge of the chemical and isotopic compositions of the Earth's upper mantle comes from the study of mantle melting products at ocean ridges. Mid-ocean ridge basalts (MORB) and abyssal peridotites (AP) are such two products. MORB represent the melt that solidifies to form the ocean crust whereas AP are the residue accreting new growth of the lithospheric mantle. Studies of the two products are expected to reveal consistent information, but if not, some hidden processes must be at work and need understanding. For example, it is considered that MORB have a uniform iron (Fe) isotope composition of $\delta^{56}Fe = +0.105 \pm 0.006‰$ ($2\,SD/\sqrt{n}$, $n = 43$)[1] irrespective of the extent of mantle melting and magma differentiation. On the other hand, AP have a mean $\delta^{56}Fe$ value of $+0.010 \pm 0.014‰$ ($2\,SD/\sqrt{n}$, $n = 37$)[2], which is indistinguishable from chondrites[3,4]. A contrast of ~0.1‰ exists between MORB and AP. Partial melting[2,5–7] and fractional crystallization[8,9] have been proposed to explain this contrast. Recent studies suggested that the partial melting process alone cannot explain this contrast[8,10].

As the erupted MORB are not primary mantle melts, but final products of primary melts that have evolved primarily through varying extent of fractional crystallization in the deep crust. We thus hypothesize that fractional crystallization-dominated MORB melt evolution is the very process that produces elevated $\delta^{56}Fe$ values of sampled MORB melts. Investigation of a suite of source homogeneous MORB melts with well-defined liquid lines of descent (LLDs) will be useful[9], but MORB are a homogenized mix of variably evolved melts through open-system magma chamber processes[11–15] with important details averaged out. Therefore, magma chamber rocks of cumulate origin, once solidified, are largely isolated from subsequent magma chamber processes (i.e., replenishment, crystallization, mixing, and eruption), and thus record in great fidelity of magma chamber processes on mineral crystal scales. In order to better understand the effect of fractional crystallization on MORB Fe isotope variation, we choose to study magma chamber rocks preserved in the lower ocean crust to test this hypothesis. The Ocean Drilling Project (ODP) Hole 735B is so far the only long in situ section of the lower ocean crust ever drilled[16]. These core samples have been thoroughly studied and well-characterized to record details of MORB melt evolution dominated by fractional crystallization[17–20].

The ODP Hole 735B (32°43′S, 57°17′E) is located on the Atlantis Bank, a wave-cut platform on the east side of the Atlantis II Fracture Zone, ~93 km south of the present-day Southwest Indian Ocean Ridge (SWIR) axis (Fig. 1). It has a total penetration of 1508 m below the seafloor (mbsf) drilled during Leg 118 and Leg 176. The SWIR separates the African and Antarctic plates with a half spreading rate of ~8 mm/year[21], which is classified as a slow- and ultraslow-spreading ridge[22]. The Hole 735B drill cores are dominated by gabbros and gabbroic rocks crosscut by minor felsic veins[16].

The large and systematic Fe isotope variation of cumulate gabbros with varying modal mineralogy and highly evolved felsic veins from Hole 735B proves the prediction and argument that the magma chamber rocks record details of Fe isotope fractionation in response to MORB melt evolution dominated by fractional crystallization.

## Results

**Samples**. The gabbroic rocks (including troctolite, olivine gabbro, gabbro, oxide gabbro, and gabbronorite) are mineralogically dominated by plagioclase and clinopyroxene with a varying abundance of olivine and Fe–Ti oxides (Supplementary Fig. 1a–c). Most of the felsic veins are quartz diorite with minor diorite, trondhjemite, and tonalite[17,20], mainly consisting of plagioclase, quartz, and amphibole with varying amounts of Fe–Ti oxides (Supplementary Fig. 1d). The Fe–Ti oxide minerals are ilmenite (Supplementary Fig. 1e) in all the samples but FV62-15 where magnetite occurs as intergrowth with ilmenite (Supplementary Fig. 1f).

We selected a set of 20 representative samples (Supplementary Data 1) covering a compositional spectrum of gabbroic rocks and felsic veins (Supplementary Figs. 1 and 2) from the drill cores and analyzed Fe isotope compositions of bulk rock samples and major Fe-bearing mineral separates (olivine, pyroxene, amphibole, and Fe–Ti oxides) of some larger samples. No plagioclase was analyzed because it has low $FeO^T$ (average of 0.23 wt%[17]) and contributes little to the bulk rock $\delta^{56}Fe$ compositions (see "Methods" section) although it is the most abundant mineral in the drill cores. Samples used in this study have been fully characterized for their mineralogy, and major and trace element compositions[17,20].

**Fe isotope compositions of ODP Hole 735B samples**. Bulk rock Fe isotope, major and trace element compositions for the studied

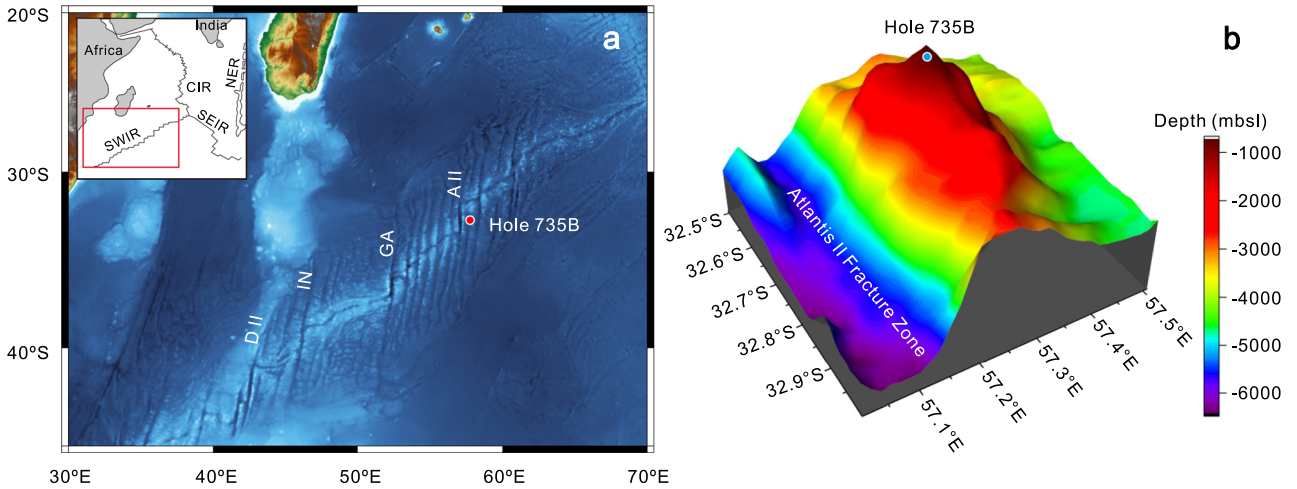


**Fig. 1 Location of the ODP Hole 735B. a** Bathymetric map of the Southwest Indian Ridge showing the location of ODP Hole 735B. The map is made using Generic Mapping Tools (GMT[65]). Topography was taken from ETOPO1 1 arc-minute Global Relief Model (https://doi.org/10.7289/V5C8276M). CIR, SWIR, and SEIR refer to Central, Southwest, and Southwest Indian Ridge; NER, Ninety East Ridge; A II, Atlantis II Fracture Zone; GA, Gallieni Fracture Zone; IN, Indomed Fracture Zone; D, Discovery II Fracture Zone. **b** Three-dimensional topography of the Atlantis Bank is made using the topography data of study[66].

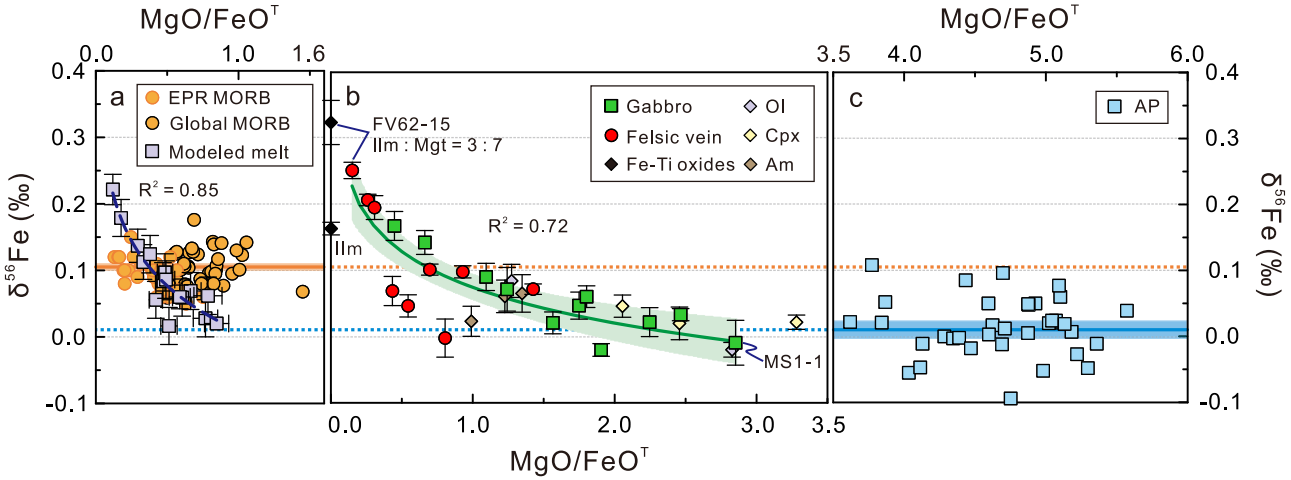


**Fig. 2 Iron isotope composition ($\delta^{56}$Fe) versus MgO/FeO$^T$ for different lithologies from ocean lithosphere. a** Global MORB[1,7,9] (orange circles). **b** Gabbro (green squares) and felsic vein (red circle) samples, as well as mineral, separate from Hole 735B of this study. **c** Global AP[2] (blue squares). MORB are considered to have uniform Fe isotope composition ($\delta^{56}$Fe = +0.050 to +0.176‰) with a mean of +0.105 ± 0.006‰[1] (orange dashed line). AP, as MORB mantle melting residues, have lighter iron isotope composition ($\delta^{56}$Fe = −0.094 to +0.108‰) with a mean of +0.010 ± 0.014‰[2] (blue dashed line). The bulk rock gabbro and felsic vein samples have Fe isotope compositions varying as low as those of AP and as high as and even higher than those of MORB. The modeled compositions (purple squares) of melt (Supplementary Data 4) in equilibrium with gabbroic samples and olivine, pyroxene therein are plotted **a** for comparison (see "Methods" section for model details). The mineral separates such as olivine (Ol, purple diamonds), clinopyroxene (Cpx, yellow diamonds), amphibole (Am, brown diamonds), and Fe–Ti oxides (black diamonds) also show a similar negative correlation between $\delta^{56}$Fe and MgO/FeO$^T$ (**b**). The best-fit lines at 95% confidence intervals with $R^2$ values are given for the calculated melt (**a**) and bulk rock samples (**b**). Error bars are ±1 SD.

samples are given in Supplementary Data 1 and 2. The bulk rock Fe isotope compositions with a large range ($\delta^{56}$Fe = −0.020–+0.252‰) show weak/no correlation with most elements (e.g., $SiO_2$, CaO, $Na_2O$, Ni, Y, and rare earth elements, with correlation coefficients |R| < 0.5, Supplementary Fig. 3), but strong negative correlation with Mg# ($R^2 = 0.72$, at >99% confidence level) (Supplementary Fig. 3d) and MgO/FeO$^T$ ($R^2 = 0.72$, at >99% confidence level) (Fig. 2b). In this study, we use MgO/FeO$^T$ instead of Mg# (=Mg/[Mg+$Fe^{2+}$]) for discussion to avoid arbitrary assumptions on $Fe^{2+}$/[$Fe^{2+}$+$Fe^{3+}$] for different rock types and samples, so that all these samples/data (MORB, gabbroic rocks, felsic veins, and AP) can be compared. Most of the mineral separates also show a similar negative correlation between $\delta^{56}$Fe and MgO/FeO$^T$ just like the bulk rock (fall in 95% confidence intervals, Fig. 2b). Compared to Fe–Ti oxides and amphibole, the $\delta^{56}$Fe of olivine and pyroxene are closer to those of the bulk rock (Supplementary Fig. 4).

## Discussion

Previous studies have shown that most of the gabbros are cumulates with bulk compositions determined largely by modal proportions of clinopyroxene and plagioclase with varying small amounts of trapped melt[17], and that the felsic veins are mixtures of residual melt with incompletely segregated crystals[20]. Unlike incompatible trace elements, iron is a major element in most rocks. It controls and contributes to the phase equilibria, and only significant mass transfer processes are able to shift its isotope composition[8]. Though some evidence shows that the reactive porous flow may occur in gabbros of the Hole 735B[23–25], its low volume[24,26] hardly affects the Fe isotope composition of the gabbros. Therefore, the strong negative correlation of bulk rock $\delta^{56}$Fe with MgO/FeO$^T$ defined by the gabbroic samples with varying modal mineralogy illustrates significant Fe isotope fractionation during MORB melt evolution dominated by fractional crystallization (Fig. 2b). Using reasonable mineral-melt isotope fractionation factors (see Supplementary Table 1 and "Methods" section)[27], we can model the Fe isotope composition of melts in equilibrium with these gabbroic samples (Fig. 2a). The result confirms the notion that fractional crystallization of olivine and clinopyroxene with lighter Fe isotope can elevate $\delta^{56}$Fe of the residual melt[9,28,29]. The progressive crystallization of olivine and clinopyroxene also increases FeO$^T$ and $TiO_2$, but decreases MgO and MgO/FeO$^T$ in the residual melt (Figs. 2 and 3) until ilmenite (ilmenite-dominated Fe–Ti solid solutions) begin to crystallize, upon which $SiO_2$ increases rapidly while $TiO_2$ declines in the residual melt (Fig. 3a–c). It is important to note that $\delta^{56}$Fe continues to increase in the residual melt throughout the crystallization sequence (Fig. 3d). Mixing between incompletely segregated crystals and residual melt can produce intermediate MgO/FeO$^T$ and $\delta^{56}$Fe compositions that lie between the compositions of the residual melt and cumulate (Fig. 2b). This is particularly obvious for the three highly evolved FV samples having high $SiO_2$ contents and incompletely segregated ilmenite (Supplementary Fig. 1d) with low $\delta^{56}$Fe.

The Fe–Ti oxides are compositionally uniform and rapidly cooled liquidus phases[20], which differ from slowly cooled exsolution aggregates in mafic layer intrusion[30,31]. Importantly, the Fe–Ti oxides are almost pure ilmenite[32] (Fe–Ti solid solutions with 91% molar ilmenite, Supplementary Fig. 1e and Data 3), which has lighter Fe than the equilibrium melt with $\Delta^{56}Fe_{ilmenite\text{-}melt} = -0.07‰$ (see "Methods" section and Supplementary Table 1). Magnetite is rare and is only found in one sample (FV62-15) as intergrowth with ilmenite (molar magnetite: ilmenite ratio of 7:3, Supplementary Fig. 1f), which would have a slightly heavier Fe than the melt with net $\Delta^{56}Fe_{Fe\text{-}Ti\ oxides\text{-}melt} = 0.08‰$ if $\Delta^{56}Fe_{magnetite\text{-}melt} = 0.11‰$ is applied (see Eqs. (6–8) in "Methods" section and Supplementary Table 1). The melt in equilibrium with these Fe–Ti oxides, which represents the very late-stage product of mid-ocean ridge basaltic magma evolution[20], would have $\delta^{56}$Fe = +0.24 ± 0.02‰ (see "Methods" section and Supplementary Data 4). Therefore, the $\delta^{56}$Fe of residual melt continues to increase with fractional crystallization of olivine, plagioclase, clinopyroxene, and ilmenite. It is important to note that despite the decreasing FeO and $TiO_2$ and increasing $SiO_2$ in the residual melt as the result of oxide

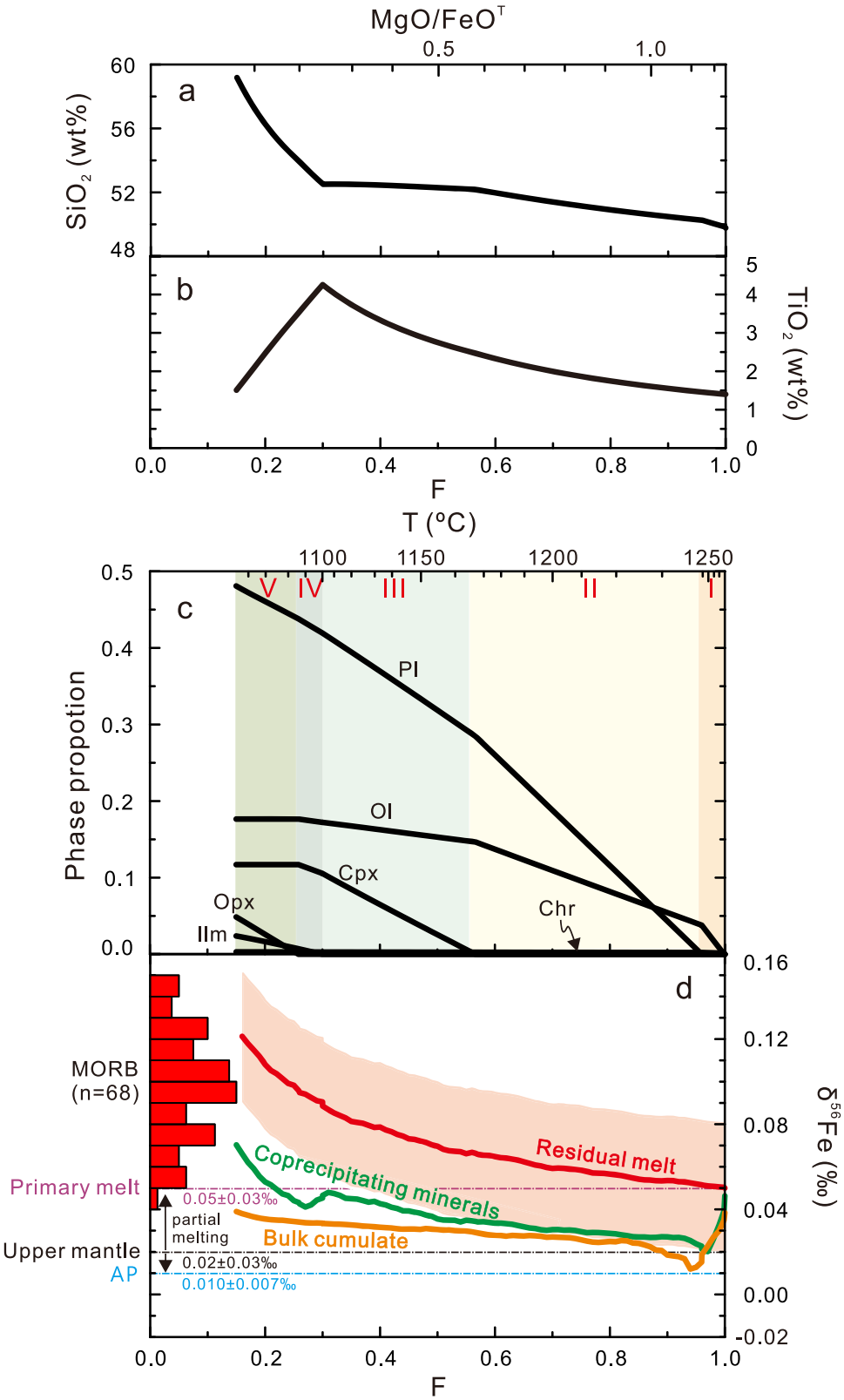


crystallization, the $\delta^{56}$Fe of the residual will not decrease, but increase, because the Fe–Ti oxide is ilmenite ($TiFeO_3$) dominated solid solution (Fig. 3; see above), which differs from the conclusion based on the study of variably evolved MORB melts by assuming liquidus oxides of titanomagnetite[9]. Crystallization of magnetite ($FeO{\cdot}Fe_2O_3$) dominated solid solution with heavier Fe will result in $\delta^{56}$Fe decrease in the residual melt[29]. The continued increase of $\delta^{56}$Fe with decreasing $MgO/FeO^T$ (Fig. 2b) is thus expected because liquidus oxides in Hole 735B are essentially all ilmenite or ilmenite-dominated solid solutions (see above)[17]. This new observation is also consistent with the modeling that it is ilmenite, not magnetite, that is on the liquidus at the oxygen fugacity quartz-fayalite-magnetite (QFM) buffer most appropriate for MORB[33] (Fig. 3c). Magnetite is expected to crystallize at lower temperatures when the MORB melt

**Fig. 3 Iron isotope fractionation during fractional crystallization of primitive MORB. a–c** Liquid lines of descent for a SWIR MORB melt[59] (corrected to Mg# = 0.72; Supplementary Table 3) modeled using Petrolog3[34] at a pressure of 0.2 GPa and oxygen fugacity at QFM buffer (see "Methods" section for model details). With decreasing temperature, chromium spinel (Chr) crystallizes first, followed by olivine (Ol), plagioclase (Pl), clinopyroxene (Cpx), ilmenite (Ilm), and orthopyroxene (Opx). The corresponding cumulate rocks are chromite-bearing dunite (I), troctolite (II), gabbro (III), oxide gabbro (IV), and oxide gabbronorite (V). With the QFM oxygen buffer, magnetite does not appear on the liquidus, which is consistent with the observation that the oxides are ilmenite-dominated solid solutions (little magnetite) throughout Hole 735B. With progressive crystallization of Ol, Pl, and Cpx, $TiO_2$ becomes concentrated in the residual melt, which leads to the crystallization of ilmenite and elevation of $SiO_2$ in the residual melt. **d** Modeling of $\delta^{56}$Fe variation in the residual melt (red line), coprecipitating minerals (green line) and bulk cumulate (orange line) during MORB melt evolution from the primitive melt with $\delta^{56}$Fe = +0.05 ± 0.03‰ (5–15% melting of the mantle with $\delta^{56}$Fe = +0.02 ± 0.03‰). See the "Methods" section and Supplementary Table 2 for modeling details. The $\delta^{56}$Fe of the residual melt increase with successive crystallization/removal of these liquidus phases with lighter Fe. The $\delta^{56}$Fe of the coprecipitating minerals in equilibrium with the more evolved melt also increases, contributing to the gentle $\delta^{56}$Fe increase of the bulk cumulate. With source heterogeneity, hence the possible variation of primary melt composition, considered, fractional crystallization can effectively explain the range of MORB $\delta^{56}$Fe[1,7,9]. Five-point moving averaging is applied for **d**.

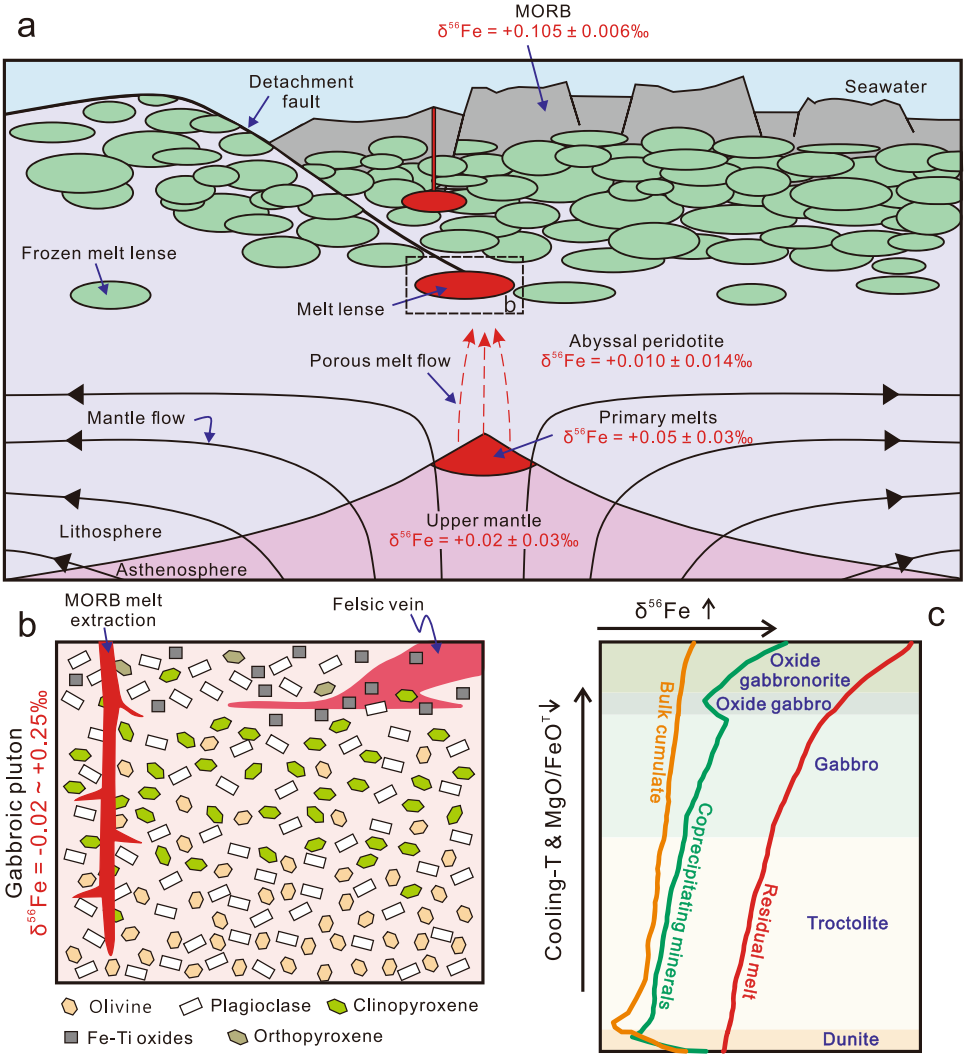


**Fig. 4 Schematic illustrations (not to scale) showing Fe isotope variation in the seafloor lithosphere in the context of MORB melt formation, migration, and crystallization. a** "Multiple injections and thin melt lenses" mode of ocean crust accretion at the SWIR[16,17,19,20]. **b** Snapshot of fractional crystallization in single melt lens. **c** Idealized scenario of MORB melt Fe isotope evolution as the result of fractional crystallization and cumulate formation. The $\delta^{56}$Fe of MORB melt increases with successive crystallization/cumulation of chromium spinel, olivine, plagioclase, clinopyroxene, and Fe–Ti oxides (dominant by ilmenite). The $\delta^{56}$Fe of the bulk cumulate keeps slowly increasing also because of the addition of liquidus minerals in equilibrium with the more evolved MORB melt with higher $\delta^{56}$Fe. However, the $\delta^{56}$Fe of the bulk ocean crust remains the same as the primary MORB melt across the Moho.

is about to solidify or the melt may be brought back up to crystallize gabbro or even troctolite by the replenishment of a new batch of melt in open-system magma chambers. The data and observations thus indicate that MORB melt evolution will rarely reach the condition of magnetite crystallization. Consequently, MORB melt evolution will be accompanied by continued $\delta^{56}$Fe increase, not decrease, throughout the entire history of MORB melt evolution (Figs. 3d and 4c). This is an important finding. In this context, we predict that basaltic melts with high water contents and higher oxygen fugacity (higher than QFM) may facilitate earlier

crystallization of magnetite and associated $\delta^{56}$Fe decrease in the residual melt (e.g., subduction-zone magmatism). The effect of oxygen fugacity on Fe isotope fractionation has been speculated in the literature[29].

To better illustrate Fe isotope fractionation during fractional crystallization of MORB melt, we modeled the LLDs using Petrolog3[34] (see "Methods" section), showing that the $\delta^{56}$Fe of the coprecipitating minerals and residual melt increases in response to continued cooling and crystallization of the MORB melt (Fig. 3) as our data (Fig. 2b) show in support of a recent study[9]. We can thus conclude that Fe isotope fractionation continues throughout MORB melt evolution, and the lower ocean crust cumulates record this process in great detail.

Bulk rock gabbro and felsic vein samples have varying $\delta^{56}$Fe values as low as those of AP and as high as and even higher than those of MORB (Fig. 2). By assuming primary MORB melt representing 5–15% melting of a mantle with $\delta^{56}$Fe = +0.02 ± 0.03‰[2,3,7], we obtain the Moho-crossing melt (ultimately solidified to form the bulk ocean crust) with $\delta^{56}$Fe of +0.05 ± 0.03‰ (Figs. 3d, 4 and Supplementary Table 2). This confirms the previous study that the Fe isotope composition of primary MORB melt would be only slightly heavier than the mantle source[8–10], and the mantle melting residues would be slightly lighter[2]. It is worth mentioning that AP are not simple melting residues but have excess olivine and incompatible elements[35–38] added during melt ascent through the advanced residues atop the mantle, causing AP to have large compositional heterogeneity on hand specimen scales[38], which explains the large $\delta^{56}$Fe variation (Fig. 2c), but the mean composition is arguably significant. With mantle source heterogeneity considered[39,40], the Moho-crossing melt must also vary, but the mean value of $\delta^{56}$Fe of +0.05 ± 0.03‰ remains the logical and reasonable approximation for primary MORB melt (Fig. 3d). The 20–80% fractional crystallization of such primary MORB melt can effectively explain the $\delta^{56}$Fe range of MORB (Fig. 3d). Successive fractional crystallization of olivine, pyroxene, and ilmenite with lighter Fe (lower $\delta^{56}$Fe) results in a progressive increase of $\delta^{56}$Fe in the residual melt, in the coprecipitating minerals in equilibrium with the evolving melt and in the bulk cumulate. The bulk cumulate with significantly lower $\delta^{56}$Fe characterizes the lower ocean crust (Figs. 3 and 4).

Note that, by mass balance, the elevated $\delta^{56}$Fe of the sampled MORB melts is complemented by the low $\delta^{56}$Fe of the lower crust cumulate rocks (Fig. 3d). Therefore, fractional crystallization of MORB melt in the deep ocean crust results in the Fe isotope contrast between MORB and AP. We should also note some subtleties. The lower ocean crust made up of cumulate rocks must have $\delta^{56}$Fe lower than the $\delta^{56}$Fe of Moho-crossing melt, but it must be heterogeneous because of varying amount of trapped melt and locally highly evolved felsic vein lithologies (Fig. 2b), leading to some lower crustal samples having somewhat higher $\delta^{56}$Fe than the model bulk cumulate (Fig. 3d). By assuming the ocean crust comprising 40% MORB melts (lavas + dikes) and 60% cumulate lower crust, we have approximately $\delta^{56}\mathrm{Fe}_{\text{[BULK OCEAN CRUST]}} = \delta^{56}\mathrm{Fe}_{\text{[PRIMARY MORB MELT]}} = 40\%\ \delta^{56}\mathrm{Fe}_{\text{[AVERAGE MORB]}} + 60\%\ \delta^{56}\mathrm{Fe}_{\text{[LOWER CRUST CUMULATE]}} = +0.05 \pm 0.03‰$.

In sum, the data (Fig. 2) and quantitative understanding (Fig. 3) demonstrate that MORB melts periodically erupted from magma chambers of the varying extent of fractional crystallization have variably higher $\delta^{56}$Fe than that of the Moho-crossing primary mantle melt, which explains in simple clarity that fractional crystallization causes the Fe isotope contrast between MORB and AP (Fig. 4).

## Methods

**Fe isotope analysis**. The studied samples were selected from the drill cores during Leg 176[17]. Sample information is given in Supplementary Data 1. Analytical methods, standards, and data for major and trace elements have been detailed[17,20]. All suspicious surface contaminants such as pen marks, saw marks, and sticker residues were thoroughly removed. The samples were then reduced to 1–2 cm size fragments and ultrasonically cleaned in Milli-Q water before being dried and grinded into powder using an agate mill in a clean environment. Some larger samples were crushed into 40–100 mesh for handpicking mineral separates under a binocular. Major Fe-bearing minerals (e.g., olivine, pyroxene, amphibole, and Fe–Ti oxides) were separated for Fe isotope analysis (Supplementary Fig. 4). Plagioclase and quartz with little Fe were not analyzed. Mineral separates were cleaned in Milli-Q water for 10 min, at least three times, in an ultrasonic bath. The iron isotope analysis was done in the Laboratory of Ocean Lithosphere and Mantle Dynamics, Institute of Oceanology, Chinese Academy of Sciences. About 5–20 mg of samples were dissolved in distilled $HNO_3$ + HCl +HF mixture in a 10 ml PFA Teflon beaker at 190 °C for 15 h, and then re-dissolved, after evaporation, with distilled 3 N $HNO_3$ for 2 h until complete dissolution. Iron was purified with a polypropylene column filled with 1 ml AG-MP-1 M resin (200–400 mesh) in a 9 N HCl medium following the procedure[41], which was improved upon previous methods[42–44]. Iron was collected using 1.5 ml 1 N HCl. The total procedural blank for these samples is 32 ng, which is negligible compared to the amount of material processed. The purified solutions were doped with GSB Ni standard (an ultrapure single elemental standard solution from the China Iron and Steel Research Institute) as an internal mass bias monitor with Ni: Fe ratio of ~1.4: 1[41].

The iron isotope compositions were determined using Nu plasma II multiple collector-inductively coupled plasma-mass spectrometer (MC-ICP-MS) in wet plasma mode with medium resolution (a mass resolution >7500). Reference material GSB Fe standard (a substitution of IRMM-014; $\delta^{56}\mathrm{Fe}_{\mathrm{IRMM\text{-}014}} = \delta^{56}\mathrm{Fe}_{\mathrm{GSB}} + 0.729$, $\delta^{57}\mathrm{Fe}_{\mathrm{IRMM\text{-}014}} = \delta^{57}\mathrm{Fe}_{\mathrm{GSB}} + 1.073$[45]) was used for bracketing each sample. Iron isotope compositions are reported as δ-notation relative to the international standard of IRMM-014: $\delta^{i}\mathrm{Fe}(‰) = [(^{i}\mathrm{Fe}/^{54}\mathrm{Fe})_{\mathrm{sample}}/(^{i}\mathrm{Fe}/^{54}\mathrm{Fe})_{\mathrm{IRMM-014}}] \times 1000$, where $i$ refers to mass 56 or 57. Our analyzed $\delta^{56}$Fe values for USGS standards agree well with recommended values in the literature[4,45]: GSP-2 (0.14 ± 0.05‰; 2 SD, $n$ = 12), BCR-2 (0.05 ± 0.07‰; 2 SD, $n$ = 8), AGV-2 (0.09 ± 0.07‰; 2 SD, $n$ = 12) and BHVO-2 (0.13 ± 0.07‰; 2 SD, $n$ = 12).

**Mineral composition analysis**. Major and minor element compositions of olivine, clinopyroxene, amphibole, and Fe–Ti oxides were analyzed on polished thin sections using a JEOL Electron Probe Micro analyzer (EPMA 8230) at the Laboratory of regional geology and resources research institute of Hebei Province. An accelerating voltage of 15 kV, a beam current of 20 nA, and a beam diameter of 1 μm were employed. For major elements, the analytical precision is better than 2%. The data are given in Supplementary Data 3.

**Calculation of $\Delta^{56}\mathrm{Fe}_{\mathrm{mineral\text{-}melt}}$**. The theory states that the heavy Fe isotope is preferentially partitioned into the phase with the highest bond strength or bond stiffness[10,27,46]. Ferric iron ($Fe^{3+}$) is predicted to have heavier Fe (i.e., higher $\delta^{56}$Fe) because the smaller ionic radii and higher valence state of Fe results in shorter and stronger bonds[10]. Fe isotope can fractionate when iron incorporates into different phases, leading to different $\delta^{56}$Fe between different phases. The fractionation between crystallizing mineral and melt is expressed as $\Delta^{56}\mathrm{Fe}_{\mathrm{mineral\text{-}melt}}$ ($=\delta^{56}\mathrm{Fe}_{\mathrm{mineral}} - \delta^{56}\mathrm{Fe}_{\mathrm{melt}}$), which is inversely proportional to temperature and is calculated using the following Eq. (1)[27]:

$$\Delta^{56}\mathrm{Fe}_{\mathrm{mineral-melt}} = 2904\frac{K_{\mathrm{mineral}} - K_{\mathrm{melt}}}{T^2}, \quad (1)$$

where $K$ is the force constant and $T$ is the temperature in Kelvin. The force constants of chromite, olivine, plagioclase, pyroxene, ilmenite, magnetite, and melt are given in Supplementary Table 1.

The coordination and valence state of Fe are the two very factors that control the bond strength and affect the Fe isotope fractionation[10,27,46]. According to previous studies[10,27,47–49], $Fe^{2+}$ and $Fe^{3+}$ are in V- or VI-fold average coordination in the basaltic melt, and in IV-fold average coordination in the rhyolitic melt, so the force constant of the rhyolitic melt is higher than in basaltic melt at given $Fe^{3+}/\Sigma Fe$. In this study, we focus on the basaltic melt. During MORB evolution, $Fe^{3+}/\Sigma Fe$ increases because $Fe^{3+}$ (vs. $Fe^{2+}$) behaves as a slightly "incompatible element"[33] until magnetite ($Fe^{2+}O \cdot Fe^{3+}_2O_3$) may begin to crystallize. However, the liquidus oxides in Hole 735B are ilmenite ($TiFe^{2+}O_3$) and ilmenite-dominated solid solutions (~molar 91%), which means that the $Fe^{3+}/\Sigma Fe$ of MORB melt is low and hardly reaches magnetite saturation. Hence, we apply a constant force constant (223 ± 17 N/m, by assuming melt $Fe^{3+}/\Sigma Fe = 0.16$[50] following the previous study[10]) for melt during MORB evolution.

Force constants for minerals (Supplementary Table 1) are taken from the literature[10,27,51] except for plagioclase. With no experimental data, we estimated the force constant for plagioclase using an empirical equation[27] by assuming $Fe^{3+}/\Sigma Fe = 0.7$ and a coordination number of 4[52]. The calculated $\Delta^{56}\mathrm{Fe}_{\mathrm{Ol\text{-}melt}}$ and $\Delta^{56}\mathrm{Fe}_{\mathrm{Pl\text{-}melt}}$ differs from the values obtained from natural samples (e.g., $\Delta^{56}\mathrm{Fe}_{\mathrm{Ol\text{-}melt}} = -0.1$ to −0.3‰[28]; $\Delta^{56}\mathrm{Fe}_{\mathrm{Pl\text{-}Mgt}} = 0.022{*}\mathrm{Ab} - 1.15$[53], where Ab is albite mode of plagioclase). Significant Fe isotope difference between olivine and melt was observed from phenocrysts and matrix glass of the Hawaiian Kilauea Iki lava[28]. However, the subsequent studies indicate that these olivine-melt pairs are not in equilibrium and the diffusive processes cause Fe isotope fractionation[10,54–56]. A previous study[53] suggests that feldspar has heavier Fe isotope composition than its coexisting

magnetite. However, these data are limited to plagioclase with high Ab and alkali feldspars, which may be applicable for plagioclase in felsic vein samples but unsuitable for plagioclase in the gabbroic samples (with an average of 42% Ab[17]).

**Calculation of melt composition in equilibrium with the gabbroic samples**. Studies on Hole 735B gabbroic rocks show significant correlations of anorthite (An) content in plagioclase with Mg# in olivine, clinopyroxene, and orthopyroxene, indicating that the bulk of the coexisting minerals in each sample were coprecipitated from a common liquid undergoing cooling[17]. Using the Fe–Mg exchange relationship between liquid and olivine[57]

$$\mathrm{Kd}^{\mathrm{Fe-Mg}}_{\mathrm{Ol-liq}} = \left(\mathrm{X}^{\mathrm{Ol}}_{\mathrm{FeO}} \times \mathrm{X}^{\mathrm{liq}}_{\mathrm{MgO}}\right) / \left(\mathrm{X}^{\mathrm{liq}}_{\mathrm{FeO}} \times \mathrm{X}^{\mathrm{Ol}}_{\mathrm{MgO}}\right) = 0.30, \quad (2)$$

we can calculate $\mathrm{MgO/FeO^T}$ of basaltic melts in equilibrium with olivine. The liquidus temperatures of olivine and basaltic melts are derived from well-established experimental petrology data summarized in study[17], from which we use the modified equation relevant to MORB melt evolution

$$T_{\mathrm{liquidus}}(^{\circ}\mathrm{C}) = 1055.1 + 193.8 \times \left(\mathrm{MgO/FeO}^T\right)_{\mathrm{melt}} - 46.966 \times \left(\mathrm{MgO/FeO}^T\right)^2_{\mathrm{melt}} \quad (3)$$

to calculate the liquidus temperature of olivine. The liquidus temperature of clinopyroxene can also be calculated using $\mathrm{Kd}^{\mathrm{Fe-Mg}}_{\mathrm{Cpx-liq}} = 0.24$[58]. Most of the gabbroic samples plot onto the band defined by the liquidus olivine and clinopyroxene, suggesting that the bulk of the coexisting minerals in these samples are in equilibrium with their parental melts in terms of $\mathrm{MgO/FeO^T}$ (Supplementary Fig. 5). To calculate the compositions of basaltic melts in equilibrium with the gabbroic samples, we assume the $\mathrm{Kd}^{\mathrm{Fe-Mg}}_{\mathrm{gabbro-melt}} = 0.27 \pm 0.03$, and the result are given in Supplementary Data 4.

For the gabbroic samples, using their mineralogy, $\alpha_{\mathrm{mineral\text{-}melt}}$ and average FeO content of each minerals therein (Supplementary Table 1 and Data 4), we can calculate the $\delta^{56}$Fe of the melt (weighted mean) in equilibrium with the bulk rock sample as follow:

$$^{56/54}\mathrm{R}_{\mathrm{melt}} = {}^{56/54}\mathrm{R}_{\mathrm{BR}} / \alpha_{\mathrm{BR-melt}}, \quad (4)$$

$$\delta^{56}\mathrm{Fe} = 1000 \times \left({}^{56/54}\mathrm{R}_{\mathrm{sample}} / {}^{56/54}\mathrm{R}_{\mathrm{std}} - 1\right), \quad (5)$$

where $^{56/54}\mathrm{R}_{\mathrm{melt}}$ and $^{56/54}\mathrm{R}_{\mathrm{BR}}$ are, respectively, the $^{56}\mathrm{Fe}/^{54}\mathrm{Fe}$ isotopic compositions of the melt and bulk rock sample. The isotopic fractionation factor $\alpha$ between gabbro bulk rock and melt can be calculated using Eqs. (6–8):

$$\alpha_{\mathrm{BR-melt}} = \alpha_{\mathrm{mineral1-melt}} \times \mathrm{f}_{\mathrm{mineral1}} + \alpha_{\mathrm{mineral2-melt}} \times \mathrm{f}_{\mathrm{mineral2}} + \ldots + \alpha_{\mathrm{mineralX-melt}} \times \mathrm{f}_{\mathrm{mineralX}}, \quad (6)$$

$$\mathrm{f}_{\mathrm{mineralX}} = \mathrm{C}_{\mathrm{FeO,mineralX}} \times \mathrm{M}_{\mathrm{mineralX}} / \mathrm{C}_{\mathrm{FeO,BR}}, \quad (7)$$

$$\Delta^{56}\mathrm{Fe}_{\mathrm{mineralX-melt}} \approx 1000 \ln \alpha_{\mathrm{mineralX-melt}} \quad (8)$$

where $\mathrm{M}_{\mathrm{mineralX}}$ represents the normalized modal abundance of an individual phase within the bulk rock; $\mathrm{C}_{\mathrm{FeO,\ mineralX}}$ is the FeO content of mineralX and $\mathrm{C}_{\mathrm{FeO,\ BR}}$ is the FeO content of the gabbro bulk rock. The $\mathrm{C}_{\mathrm{FeO,\ BR}}$ are reconstructed by mineral modes and mineral compositions of gabbro (Supplementary Data 4). For simplicity, we assume reasonable temperature for different minerals in calculating the $\Delta^{56}\mathrm{Fe}_{\mathrm{mineralX\text{-}melt}}$, and the parameters are given in Supplementary Table 1.

Trapped melt in gabbros could affect Fe isotope composition of the bulk rock, but such melt, if any, is volumetrically small, petrographically invisible, and is often discussed using excess incompatible element abundances[17]. We expect that the effect of trapped melt on bulk rock Fe isotope is insignificant. In fact, the Fe isotope composition of minute trapped melt, if present, is already incorporated in the bulk rock compositions (Fig. 2b) that are largely controlled by the major mineralogy. Hence, we do not make assumptions to deal with the effect of trapped melt to avoid arbitrary complications. The calculated melt in equilibrium with the gabbroic samples plots in Fig. 2a. The Fe isotope compositions of melt in equilibrium with mineral separates are also calculated using Eqs. (6–8).

For samples MS1-1 and MS79-26, the $\delta^{56}$Fe of the melts in equilibrium with bulk rocks and minerals are comparable (within error). For sample MS11-5, the $\delta^{56}$Fe of the melt in equilibrium with bulk rock is lower than the melts in equilibrium with olivine and pyroxene (Supplementary Data 4). Some important minerals must have missed. Plagioclase is ruled out because it contributes less than 0.003‰ (calculated using Eqs. (6–8) and parameters given in Supplementary Table 1 and Data 4) to the bulk rock $\delta^{56}$Fe compositions. There is a large amount of tiny ilmenite disseminated in this sample. Underestimation of the amount of ilmenite which concentrated lighter Fe isotope may result in this discrepancy.

For the felsic vein samples, their Fe isotope compositions are mainly controlled by the incompletely segregated crystals and the residual melt. Though the residual melts have low FeO contents, they are likely to have higher $\mathrm{Fe^{3+}/\Sigma Fe}$, than low-$\mathrm{SiO_2}$ and high $\mathrm{MgO/FeO^T}$ samples because of the "incompatible element" behavior of $\mathrm{Fe^{3+}}$ (vs. $\mathrm{Fe^{2+}}$)[33]. The felsic vein samples thus have heavier Fe isotope compositions. Mixing between incompletely segregated crystals and residual melt gives rise to intermediate $\mathrm{MgO/FeO^T}$ and $\delta^{56}$Fe compositions that lie between the compositions of the residual melt and cumulate (Fig. 2b). The plagioclase with high Ab may be the host of heavy Fe isotope in the solidified residual melt samples[53].

**The Fe isotope composition of the primary MORB melt**. In order to calculate Fe isotope composition of the primary MORB melt, we use a batch non-modal melting model (calculating parameters are given in Supplementary Table 2) by using a mantle source composition of $\delta^{56}\mathrm{Fe} = +0.02 \pm 0.03‰$[2,3,7] as a starting point. The $\delta^{56}$Fe of source, melt, and residue satisfy Eqs. (9–11):

$$\delta^{56}\mathrm{Fe}_{\mathrm{source}} = (\mathrm{C}_{\mathrm{FeO,melt}} \times \mathrm{F}/\mathrm{C}_{\mathrm{FeO,source}}) \times \delta^{56}\mathrm{Fe}_{\mathrm{melt}} + (1 - \mathrm{C}_{\mathrm{FeO,melt}} \times \mathrm{F}/\mathrm{C}_{\mathrm{FeO,source}}) \times \delta^{56}\mathrm{Fe}_{\mathrm{residue}}. \quad (9)$$

Using the $\Delta^{56}\mathrm{Fe}_{\mathrm{mineral\text{-}melt}}$ given in Supplementary Table 1, the $\delta^{56}$Fe of the melt can be calculated using:

$$\delta^{56}\mathrm{Fe}_{\mathrm{melt}} = \delta^{56}\mathrm{Fe}_{\mathrm{source}} - (1 - \mathrm{C}_{\mathrm{FeO,melt}} \times \mathrm{F}/\mathrm{C}_{\mathrm{FeO,\ source}}) \times \Delta^{56}\mathrm{Fe}_{\mathrm{residue-melt}} \quad (10)$$

where

$$\Delta^{56}\mathrm{Fe}_{\mathrm{residue-melt}} = (\mathrm{C}_{\mathrm{FeO,mineral1}} \times \mathrm{M}_{\mathrm{mineral1}} / \mathrm{C}_{\mathrm{FeO,residual}}) \times \Delta^{56}\mathrm{Fe}_{\mathrm{mineral1-melt}} + \ldots\ldots + (\mathrm{C}_{\mathrm{FeO,mineralX}} \times \mathrm{M}_{\mathrm{mineralX}} / \mathrm{C}_{\mathrm{FeO,residual}}) \times \Delta^{56}\mathrm{Fe}_{\mathrm{mineralX-melt}}. \quad (11)$$

**Calculation of Fe isotope fractionation during fractional crystallization**. To better understand Fe isotope fractionation during MORB melt evolution, we explore the fractional crystallization model using Petrolog3[34] with a starting composition of MORB sample (3/5c(3)) from an off-axis site nearby the Atlantis Platform[59]. This MORB composition is corrected to Mg# = 0.72 in equilibrium with mantle olivine of $\mathrm{Fo_{90}}$[12,60]. The original and corrected major element compositions are given in Supplementary Table 3. The corrected MORB melt is set to crystallize spinel, olivine, plagioclase, clinopyroxene, orthopyroxene, ilmenite, and magnetite at a pressure of 0.2 GPa and oxygen fugacity at QFM buffer (Petrolog3[34]), using the mineral-melt equilibria models[57,61–64]. A controlled amount of the crystal mass (0.01 wt%, calculation step) increases at each step of the calculation. The model stops at 15% liquid remaining. With decreasing temperature, chromium spinel crystallizes first, followed by olivine, plagioclase, clinopyroxene, ilmenite, and orthopyroxene (Fig. 3c). The $\mathrm{SiO_2}$ of residual melt does not increase until oxides (ilmenite) begin to crystallize (Fig. 3a–c). Magnetite does not appear on the liquidus to crystallize in modeling, which agrees with the observation that magnetite is rare throughout Hole 735B (Fig. 3c).

Using the result of fractional crystallization model with Petrolog3, and assuming the starting MORB melt represents the primary MORB melt with $\delta^{56}$Fe of ~+0.05 ± 0.03‰ (5–15% melting of the mantle with $\delta^{56}\mathrm{Fe} = +0.02 \pm 0.03‰$, Supplementary Table 2), the fractionation of Fe isotope for each step of MORB melt evolution can be evaluated using Eq. (12):

$$^{56/54}\mathrm{R}_{\mathrm{melt},n} = \left({}^{56/54}\mathrm{R}_{\mathrm{melt},n-1} \times \mathrm{F}_{\mathrm{melt},n-1} - {}^{56/54}\mathrm{R}_{\mathrm{CM},n} \times \mathrm{X}_{\mathrm{CM},n}\right) / \mathrm{F}_{\mathrm{melt},n}, \quad (12)$$

where $\mathrm{F}_{\mathrm{melt}}$ is mass fraction of residual melt; $\mathrm{X_{CM}}$ is mass fraction of coprecipitating minerals (CM); $n$ is the current step within the evolution of the magma and $n - 1$ represents the previous step. The fractionation of Fe isotope for coprecipitating minerals can be calculated using Eqs. (13–16):

$$^{56/54}\mathrm{R}_{\mathrm{CM},n} = \alpha_{\mathrm{CM},n} \times {}^{56/54}\mathrm{R}_{\mathrm{melt},n-1}, \quad (13)$$

where

$$\alpha_{\mathrm{CM},n} = \mathrm{f}_{\mathrm{Sp},n} \times \alpha_{\mathrm{Sp},n} + \mathrm{f}_{\mathrm{Ol},n} \times \alpha_{\mathrm{Ol},n} + \mathrm{f}_{\mathrm{Pl},n} \times \alpha_{\mathrm{Pl},n} + \mathrm{f}_{\mathrm{Cpx},n} \times \alpha_{\mathrm{Cpx},n} + \mathrm{f}_{\mathrm{Ilm},n} \times \alpha_{\mathrm{Ilm},n} + \mathrm{f}_{\mathrm{Opx},n} \times \alpha_{\mathrm{Opx},n}, \quad (14)$$

$$\mathrm{f}_{\mathrm{mineral},n} = \mathrm{C}_{\mathrm{FeO,mineral},n} \times \mathrm{X}_{\mathrm{mineral},n} / (\mathrm{C}_{\mathrm{FeO,CM},n} \times \mathrm{X}_{\mathrm{CM},n}), \quad (15)$$

$$X_{CM,n} = X_{Sp,n} + X_{Ol,n} + X_{Pl,n} + X_{Cpx,n} + X_{Ilm,n} + X_{Opx,n}, \quad (16)$$

According to Eqs. (8) and (1) as well as force constants (Supplementary Table 1), we can calculate $\alpha_{\mathrm{mineralX}}$ of each step (with different temperature). The fractionation of Fe isotope for bulk cumulate (BC) can be calculated using the mass balance Eq. (17):

$$^{56/54}\mathrm{R}_{\mathrm{BC},n} = \left({}^{56/54}\mathrm{R}_{\mathrm{melt},0} \times \mathrm{F}_{\mathrm{melt},0} - {}^{56/54}\mathrm{R}_{\mathrm{melt},n} \times \mathrm{F}_{\mathrm{melt},n}\right) / \left(\mathrm{F}_{\mathrm{melt},0} - \mathrm{F}_{\mathrm{melt},n}\right) \quad (17)$$

The modeling result is shown in Fig. 3d.

## Data availability

Topography data for Fig. 1a (ETOPO1 1 arc-minute Global Relief Model) and Fig. 1b[66] are available at the NOAA National Centers for Environmental Information (https://www.ncei.noaa.gov/). Other relevant data necessary to reproduce the figures presented in this paper are available in supplementary files and references given in the captions. Data are also available on the Figshare Data repository at https://doi.org/10.6084/m9.figshare.14135021.v1.

## Code availability

Petrolog3 is available for free download from http://petrolog.web.ru/. Figure 1a was plotted using GMT6.0, which can be accessed at https://www.generic-mapping-tools.org/.

Received: 11 August 2020; Accepted: 1 March 2021;
Published online: 25 March 2021

## References

1. Teng, F. Z., Dauphas, N., Huang, S. & Marty, B. Iron isotopic systematics of oceanic basalts. *Geochim. Cosmochim. Acta* **107**, 12–26 (2013).
2. Craddock, P. R., Warren, J. M. & Dauphas, N. Abyssal peridotites reveal the near-chondritic Fe isotopic composition of the Earth. *Earth Planet. Sci. Lett.* **365**, 63–76 (2013).
3. Dauphas, N. et al. Iron isotopes may reveal the redox conditions of mantle melting from Archean to Present. *Earth Planet. Sci. Lett.* **288**, 255–267 (2009).
4. Craddock, P. R. & Dauphas, N. Iron isotopic compositions of geological reference materials and chondrites. *Geostand. Geoanal. Res.* **35**, 101–123 (2011).
5. Williams, H. M. et al. Systematic iron isotope variations in mantle rocks and minerals: the effects of partial melting and oxygen fugacity. *Earth Planet. Sci. Lett.* **235**, 435–452 (2005).
6. Weyer, S. et al. Iron isotope fractionation during planetary differentiation. *Earth Planet. Sci. Lett.* **240**, 251–264 (2005).
7. Weyer, S. & Ionov, D. A. Partial melting and melt percolation in the mantle: the message from Fe isotopes. *Earth Planet. Sci. Lett.* **259**, 119–133 (2007).
8. Sossi, P. A., Nebel, O., Anand, M. & Poitrasson, F. On the iron isotope composition of Mars and volatile depletion in the terrestrial planets. *Earth Planet. Sci. Lett.* **449**, 360–371 (2016).
9. Chen, S. et al. Iron isotope fractionation during mid-ocean ridge basalt (MORB) evolution: evidence from lavas on the East Pacific Rise at 10° 30′ N and its implications. *Geochim. Cosmochim. Acta* **267**, 227–239 (2019).
10. Dauphas, N. et al. Magma redox and structural controls on iron isotope variations in Earth's mantle and crust. *Earth Planet. Sci. Lett.* **398**, 127–140 (2014).
11. Batiza, R. & Niu, Y. L. Petrology and magma chamber processes at the East Pacific Rise ~9°30'N. *J. Geophys. Res.* **97**, 6779–6797 (1992).
12. Niu, Y. L. The meaning of global ocean ridge basalt major element compositions. *J. Petrol.* **57**, 2081–2104 (2016).
13. O'Hara, M. J. Are ocean floor basalts primary magma? *Nature* **220**, 683–686 (1968).
14. O'Neill, H. S. C. & Jenner, F. E. The global pattern of trace-element distributions in ocean floor basalts. *Nature* **491**, 698–704 (2012).
15. Coogan, L. A. & O'Hara, M. J. MORB differentiation: In situ crystallization in replenished-tapped magma chambers. *Geochim. Cosmochim. Acta* **158**, 147–161 (2015).
16. Dick, H. J. et al. A long in situ section of the lower ocean crust: results of ODP Leg 176 drilling at the Southwest Indian Ridge. *Earth Planet. Sci. Lett.* **179**, 31–51 (2000).
17. Niu, Y., Gilmore, T., Mackie, S., Greig, A., & Bach, W. in *Proceedings of the Ocean Drilling Program, Scientific Results* (eds Natland, J. H., Dick, H. J. B., Miller, D. J., & Von Herzen, R. P.) 1–60 (2002).
18. Dick, H. J., et al. in *Proceedings of the Ocean Drilling Program, Scientific Results* (eds Natland, J. H., Dick, H. J. B., Miller, D. J., & Von Herzen, R. P.) 1–60 (2002).
19. Stone, S. & Niu, Y. Origin of compositional trends in clinopyroxene of oceanic gabbros and gabbroic rocks: a case study using data from ODP Hole 735B. *J. Volcanol. Geotherm. Res.* **184**, 313–322 (2009).
20. Chen, Y. et al. Petrogenesis of ODP Hole 735B (Leg 176) oceanic plagiogranite: Partial melting of gabbros or advanced extent of fractional crystallization? *Geochem. Geophys. Geosyst.* **20**, 2717–2732 (2019).
21. Robinson, P. T., Dick, H. J., Natland, J. H., & O. D. P. in *Ophiolites and Oceanic Crust: New Insights from Field Studies and Ocean Drilling Program* (eds Dilek, Y., Moores, E. M., Elthon, D., & Nicolas, A.) 75–86 (2000).
22. Dick, H. J., Lin, J. & Schouten, H. An ultralslow-spreading class of ocean ridge. *Nature* **426**, 405–412 (2003).
23. Gao, Y., Hoefs, J., Hellebrand, E., von der Handt, A. & Snow, J. E. Trace element zoning in pyroxenes from ODP Hole 735B gabbros: diffusive exchange or synkinematic crystal fractionation? *Contrib. Mineral. Petrol.* **153**, 429–442 (2007).
24. Lissenberg, C. J. & MacLeod, C. J. A reactive porous flow control on mid-ocean ridge magmatic evolution. *J. Petrol.* **57**, 2195–2220 (2016).
25. McCoy-West, A. J., Millet, M. A. & Burton, K. The neodymium stable isotope composition of the oceanic crust: reconciling the mismatch between erupted mid-ocean ridge basalts and lower crustal gabbros. *Front. Earth Sci* **8**, 25 (2020).
26. Lissenberg, C. J., MacLeod, C. J., Howard, K. A. & Godard, M. Pervasive reactive melt migration through fast-spreading lower oceanic crust (Hess Deep, equatorial Pacific Ocean). *Earth Planet. Sci. Lett.* **361**, 436–447 (2013).
27. Sossi, P. A. & O'Neill, H. S. The effect of bonding environment on iron isotope fractionation between minerals at high temperature. *Geochim. Cosmochim. Acta* **196**, 121–143 (2017).
28. Teng, F. Z., Dauphas, N. & Helz, R. T. Iron isotope fractionation during magmatic differentiation in Kilauea Iki lava lake. *Science* **320**, 1620–1622 (2008).
29. Sossi, P. A., Foden, J. D. & Halverson, G. P. Redox-controlled iron isotope fractionation during magmatic differentiation: an example from the Red Hill intrusion, S. Tasmania. *Contrib. Mineral. Petrol.* **164**, 757–772 (2012).
30. Chen, L. et al. Iron isotope fractionation during crystallization and sub-solidus re-equilibration: Constraints from the Baima mafic layered intrusion, SW China. *Chem. Geol.* **380**, 97–109 (2014).
31. Wei, Y. et al. Geochemistry and iron isotope systematics of coexisting Fe-bearing minerals in magmatic FeTi deposits: a case study of the Damiao titanomagnetite ore deposit, North China Craton. *Gondwana Res.* **81**, 240–251 (2020).
32. Natland, J. H., Meyer, P. S., Dick, H. J. B., & Bloomer, S. H. in *Proc. Ocean Drilling Program, Scientific Results* (eds Von Herzen, R. P., Robinson, P. T.) 75–111 (1991).
33. O'Neill, H. S. C., Berry, A. J. & Mallmann, G. The oxidation state of iron in Mid-Ocean Ridge Basaltic (MORB) glasses: Implications for their petrogenesis and oxygen fugacities. *Earth Planet. Sci. Lett.* **504**, 152–162 (2018).
34. Danyushevsky, L. V. & Plechov, P. Petrolog3: integrated software for modeling crystallization processes. *Geochem. Geophys. Geosyst.* **12**, 1–32 (2011).
35. Niu, Y. Mantle melting and melt extraction processes beneath ocean ridges: evidence from abyssal peridotites. *J. Petrol.* **38**, 1047–1074 (1997).
36. Niu, Y., Langmuir, C. H. & Kinzler, R. J. The origin of abyssal peridotites: a new perspective. *Earth Planet. Sci. Lett.* **152**, 251–265 (1997).
37. Niu, Y. & Hékinian, R. Basaltic liquids and harzburgitic residues in the Garrett Transform: a case study at fast-spreading ridges. *Earth Planet. Sci. Lett.* **146**, 243–258 (1997).
38. Niu, Y. Bulk-rock major and trace element compositions of abyssal peridotites: implications for mantle melting, melt extraction and post-melting processes beneath mid-ocean ridges. *J. Petrol.* **45**, 2423–2458 (2004).
39. Gleeson, M. L., Gibson, S. A. & Williams, H. M. Novel insights from Fe-isotopes into the lithological heterogeneity of Ocean Island Basalts and plume-influenced MORBs. *Earth Planet. Sci. Lett.* **535**, 116114 (2020).
40. Sun, P. et al. Large iron isotope variation in the eastern Pacific mantle as a consequence of ancient low-degree melt metasomatism. *Geochim. Cosmochim. Acta* **286**, 269–288 (2020).
41. Gong, H. et al. A re-assessment of nickel-doping method in iron isotope analysis on rock samples using multi-collector inductively coupled plasma mass spectrometry. *Acta Geochim.* **39**, 1–10 (2020).
42. Weyer, S. & Schwieters, J. High precision Fe isotope measurements with high mass resolution MC-ICPMS. *Inter. J. Mass Spectrom.* **226**, 355–368 (2003).
43. Dauphas, N., Pourmand, A. & Teng, F. Z. Routine isotopic analysis of iron by HR-MC-ICPMS: How precise and how accurate? *Chem. Geol.* **267**, 175–184 (2009).
44. Cheng, T., Nebel, O., Sossi, P. A. & Chen, F. Refined separation of combined Fe–Hf from rock matrices for isotope analyses using AG-MP-1 M and Ln-Spec chromatographic extraction resins. *MethodsX* **1**, 144–150 (2014).
45. He, Y. et al. High-precision iron isotope analysis of geological reference materials by high-resolution MC-ICP-MS. *Geostand. Geoanal. Res.* **39**, 341–356 (2015).
46. Young, E. D. et al. High-temperature equilibrium isotope fractionation of non-traditional stable isotopes: experiments, theory, and applications. *Chem. Geol.* **395**, 176–195 (2015).
47. Wilke, M. Fe in magma—an overview. *Ann. Geophys.* **48**, 609–617 (2005).
48. Jackson, W. E. et al. Multi-spectroscopic study of Fe(II) in silicate glasses: Implications for the coordination environment of Fe(II) in silicate melts. *Geochim. Cosmochim. Acta* **69**, 4315–4332 (2005).
49. Foden, J., Sossi, P. A. & Wawryk, C. M. Fe isotopes and the contrasting petrogenesis of A-, I- and S-type granite. *Lithos* **212–215**, 32–44 (2015).
50. Cottrell, E. & Kelley, K. A. The oxidation state of Fe in MORB glasses and the oxygen fugacity of the upper mantle. *Earth Planet. Sci. Lett.* **305**, 270–282 (2011).
51. Jackson, J. M., Hamecher, E. A. & Sturhahn, W. Nuclear resonant X-ray spectroscopy of (Mg, Fe)$SiO_3$ orthoenstatites. *Eur. J. Mineral* **21**, 551–560 (2009).
52. Lundgaard, K. L. & Tegner, C. Partitioning of ferric and ferrous iron between plagioclase and silicate melt. *Contrib. Mineral. Petrol.* **147**, 470–483 (2004).
53. Wu, H., He, Y., Bao, L., Zhu, C. & Li, S. Mineral composition control on inter-mineral iron isotopic fractionation in granitoids. *Geochim. Cosmochim. Acta* **198**, 208–217 (2017).
54. Teng, F., Dauphas, N., Helz, R. T., Gao, S. & Huang, S. Diffusion-driven magnesium and iron isotope fractionation in Hawaiian olivine. *Earth Planet. Sci. Lett.* **308**, 317–324 (2011).
55. Weyer, S. & Seitz, H. Coupled lithium- and iron isotope fractionation during magmatic differentiation. *Chem. Geol.* **294**, 42–50 (2012).

56. Prissel, K. B. et al. Experimentally determined effects of olivine crystallization and melt titanium content on iron isotopic fractionation in planetary basalts. *Geochim. Cosmochim. Acta* **238**, 580–598 (2018).
57. Roeder, P. L. & Emslie, R. F. Olivine-liquid equilibrium. *Contrib. Mineral. Petrol.* **29**, 275–289 (1970).
58. Langmuir, C. H., Klein, E. M., & Plank, T. in *Mantle Flow and Melt Generation at Mid-Ocean Ridges* (eds Morgan, J. P., Blackman, D. K., & Sinton, J. M.) 183–280 (1992).
59. Robinson, C. J., Bickle, M. J., Minshull, T. A., White, R. S. & Nichols, A. R. Low degree melting under the Southwest Indian Ridge: the roles of mantle temperature, conductive cooling and wet melting. *Earth Planet. Sci. Lett.* **188**, 383–398 (2001).
60. Niu, Y. & O'Hara, M. J. Global Correlations of Ocean Ridge Basalt chemistry with axial depth: a new perspective. *J. Petrol.* **49**, 633–664 (2008).
61. Ford, C. E., Russell, D. G., Groven, J. A. & Fisk, M. R. Distribution coefficients of $Mg^{2+}$, $Fe^{2+}$, $Ca^{2+}$ and $Mn^{2+}$ between olivine and melt. *J. Petrol.* **24**, 256–265 (1983).
62. Nielsen, R. L. & Drake, M. J. Pyroxene-melt equilibria. *Geochim. Cosmochim. Acta* **43**, 1259–1272 (1979).
63. Ariskin, A. A. & Barmina, G. S. An empirical model for the calculation of spinel-melt equilibria in mafic igneous systems at atmospheric pressure: 1. Chromian spinels. *Contrib. Mineral. Petrol.* **123**, 282–292 (1996).
64. Ariskin, A. A. & Barmina, G. S. An empirical model for the calculation of spinel-melt equilibria in mafic igneous systems at atmospheric pressure: 2. Fe-Ti oxides. *Contrib. Mineral. Petrol.* **134**, 251–263 (1999).
65. Wessel, P. et al. The generic mapping tools version 6. *Geochem. Geophys. Geosyst.* **20**, 5556–5564 (2019).
66. Smith, W. H. & Sandwell, D. T. Global sea floor topography from satellite altimetry and ship depth soundings. *Science* **277**, 1956–1962 (1997).


## Acknowledgements

We thank Dr. Yongsheng He for providing the GSB Fe reference material. This study is supported by the National Nature Science Foundation of China (NSFC, 41630968), the NSFC-Shandong Joint Fund for Marine Science Research Centers (U1606401), 111 Project (B18048), and NSFC (91958215, 41776067).

## Author contributions

Y.N. designed the project, Y.C. and Y.N. wrote the manuscript, Y.C. did an analysis with the assistance of M.D., H.G., and P.G.

## Competing interests

The authors declare no competing interests.

## Additional information

**Supplementary information** The online version contains supplementary material available at https://doi.org/10.1038/s43247-021-00135-5.

**Correspondence** and requests for materials should be addressed to Y.C. or Y.N.

**Peer review information** Primary handling editor: Joe Aslin.